Electrodeposited Ni-Co layered double hydroxides on titanium carbide as a binder-free electrode for supercapacitors

H. Li[a], F. Musharavati[b], E. Zalenezhad[a,*], X. Chen[a], K.N. Hui[c,*], K.S. Hui[d,*]

[a]*Department of Mechanical Convergence Engineering, Hanyang University, 222 Wangsimni-ro, Seongdong-gu, Seoul, 04763, Korea*

[b]*Mechanical and Industrial Engineering Department, College of Engineering, Qatar University, 2713, Doha, Qatar*

[c]*Institute of Applied Physics and Materials Engineering, University of Macau, Avenida da Universidade, Macau*

[d]*School of Mathematics, University of East Anglia, Norwich, NR4 7TJ, United Kingdom*

[*]Corresponding author

E-mail address: erfan@hanyang.ac.kr (E. Zalenezhad)

E-mail address: bizhui@umac.mo (K.N. Hui)

E-mail address: k.hui@uea.ac.uk (K.S. Hui)

Abstract

We report the synthesized mixture of MXene and Ni-Co LDH on nickel foam by an electrodeposition technique. The specific capacitance of the mixture attained 983.6 F g^{-1} at a discharge current of 2 A g^{-1}, which is greater than that of pure MXene. Compared to Ni-Co LDH, the sample created through electrodeposition provided a better rate capability of 983.6 F g^{-1} at 2 A g^{-1} and 536.6 F g^{-1} at 50 A g^{-1} and cycling stability with 76% retention after 5000 cycles at 30 A g^{-1}. Moreover, a solid-state asymmetric supercapacitor with MXene-LDH as the positive electrode and multi-walled carbon nanotube coated on the nickel foam as the negative electrode delivers high energy density (36.70 Wh kg^{-1} at the power density of 1.44 kW kg^{-1}), which outperforms the other devices reported previously.

1. Introduction

Electrochemical capacitors (ECs), also known as supercapacitors, have attracted increasing attention as energy storage devices in the recent years because of many advantages including higher power density, longer cycle life, and safety [1, 2]. Depending on the advantages, ECs as a new type of energy storage and conversion device have very promising applications. Based on the charge storage mechanism, there are two different categories of supercapacitors, electrochemical double layer capacitors (EDLCs) and pseudocapacitors. ELDCs are based on non-Faradaic charge separation

at the interface between the electrode and electrolyte, while pseudocapacitors are based on the Faradaic redox reaction of electroactive materials [3, 4].

Recently, MXene material had been synthesized by a wet hydrofluoric acid (HF) solution treatment from "MAX phases," and the new series of two-dimensional (2D) carbonitrides and metal carbides were promising candidates for electrode materials of supercapacitors. MXenes have a composition of $M_{n+1}X_nT_x$, in which M is an early transition metal, X represents nitrogen or carbon, n= 1, 2, or 3, and T stands for the surface functional group (e.g., O^-, OH^-, F^-) [5, 6]. To date, more than 60 different MXene compositions have been reported, such as Ti_2C, V_2C, Nb_2C, $(Ti_{0.5}Nb_{0.5})_2C$, and typical Ti_3C_2. MXenes have already shown their potential as favorable electrode materials for Li-ion batteries [7], supercapacitors [8], and sensors [9] due to their large surface area, layered structure, high electrical conductivity, environmentally-friendly characteristics, and outstanding chemical stability [5, 6, 10]. Most importantly, Ti_3C_2 is one of a few materials that exhibit pseudocapacitive behavior; hence, Ti_3C_2 is one of the most broadly studied and most favorable members of this series of supercapacitors [11, 12]. Layered double hydroxides (LDH), also named hydertalcite-like clays or anionic clays, contain stacked brucite-type octahedral layers with water molecules and anions inhabiting the interlayer space [13, 14]. Recently, these inorganic layered materials have attracted growing attention in several areas due to their appropriate properties of good catalytic activity, high thermal stability, and low cost [15-17]. And the Ni-Co LDH has been widely used for pseudocapacitors because of their versatile properties of flexible ion exchangeability, good redox activity. Particularly, Ni–Co LDH

nanosheets offer superior electrochemical properties over other nanostructures due to the interconnected arrangement and high specific surface area which allows easy contact with electrolyte ions for rapid and reversible faradic reactions [18, 19].

In this study, an electrodeposition technique was utilized to synthesize a mixture of MXene and Ni-Co LDH on nickel foam without a binder, which prevents the decrease in electrical conductivity caused by the electrical resistance of the binder. Moreover, to further evaluate the MXene-LDH electrode for practical applications, a Solid-state asymmetric supercapacitor (SASC) was fabricated using MXene-LDH@NF as the positive electrode and multiwalled carbon nanotube (MWCNT) as the negative electrode. The characterizations of the electrode were executed by energy-dispersive X-ray spectroscopy (EDS) and scanning electron microscopy (SEM). The electrochemical analyses were performed by cyclic voltammetry, electrochemical impedance spectroscopy, and galvanostatic charge-discharge.

2. Experimental Details

2.1 Synthesis of Ti_3C_2

Typically, 2D Ti_3C_2 powders were produced by immersing Ti_3AlC_2（98 wt.% pure, -100 mesh）in 49% HF at 60 °C for 24h. The powders were then rinsed with distilled water and centrifugally separated, followed by drying in a vacuum furnace at 80 °C. Then, 0.5g of the detached powders were combined with 10 ml of dimethyl sulfoxide (DMSO) for intercalation and then magnetically stirred for 24h at ambient temperature. The powders were separated from the obtained suspension by rinsing with distilled water, centrifugally separating, and drying in a vacuum furnace at 60 °C. The Ti_3C_2

intercalated with DMSO after detachment was named in- Ti_3C_2.

2.2 Fabrication of Ti_3C_2 electrodes

The Ti_3C_2 colloidal suspension was prepared by 0.1 g of in- Ti_3C_2 powders mixed with 100 ml deionized water under vigorous magnetic stirring for 4h. Nickel foam was cut into the required size (1cm x 1cm), and the surface was cleaned with alcohol. The Ti_3C_2 colloidal suspension was then dropped with a pipette onto the pretreated nickel foam sheet, which was placed on a hot plate maintained at 80 °C [5]. The Ti_3C_2 content of the whole electrode was easily controlled by adjusting the volume of the suspension.

2.3 Electrodeposition of Ni-Co LDH on the Ti_3C_2 electrode

The bimetallic (Ni, Co) hydroxide precursor was coated on the Ti_3C_2 electrode in a 10 mM $Co(NO_3)_2 \cdot 6H_2O$ and 5 mM $Ni(NO_3)_2 \cdot 6H_2O$ aqueous mixed electrolyte utilizing an electrochemical workstation [20, 21]. A conventional three-electrode system was used and was comprised of a Ti_3C_2 electrode as a working electrode, Ag/AgCl as a reference electrode, and a platinum plate as a counter electrode. The deposition was prepared using a cyclic voltammetry electrodeposition method. The experimental process was performed at a scan rate of 5 mV^{-1} for different cycles within a voltage range of -1.2 V to 0.2 V. Then, the electrode was washed with deionized water and dried in a vacuum furnace at 60 °C for 12h. The MXene and LDH support on the nickel foam without binders was considered the C-electrode. The active materials ratio of MXene to LDH is shown in Table 1.

2.4 Preparation of PVA/KOH electrolyte and MWCNT negative electrode

3 g of PVA and 3 g of KOH were dissolved in distil water with agitation at 80 °C for 5 h. After complete dissolution, the excess water was evaporated at room temperature and eventually a PVA–KOH gel electrolyte was obtained. MWCNT (80 wt.%), graphite (10 wt.%) and Polyvinylidene fluoride (PVDF, 10 wt.%) were mixed in N-Methyl pyrrolidone (NMP) [22, 23]. The resultant mixture was milled and the paste placed in the nickel-foam substrate and dried at 60 °C for 6 h.

2.5 Characterization of the LDH-MXene electrode

Powder X-ray diffraction (XRD, Bruker D8 Advance X-ray) of the samples was performed using Cu Kα radiation ($\lambda = 0.15406$nm) at 40kV and 30mA. The scanning speed was 5° min-1 with 0.02° step. The Fourier transform infrared spectroscopy (FT-IR, Nicolet 750) spectra of the samples were measured using the KBr self-supported pressing technique. The scanning range was between 400 and 4000 cm^{-1}, and the scanning time was 32 s. The structure and morphology of the specimens were examined using X-ray photoelectron spectroscopy (XPS, Al Kα excitation laser, ESCA2000) and field emission scanning electron microscopy (FESEM, LEO-1550) with an applied voltage of 5 kV and energy-dispersive X-ray spectroscopy (EDS). Transmission electron microscopy (TEM) and selected area electron diffraction (SAED) were performed using JEM-2100F (JEOL) at an acceleration voltage of 200 kV.

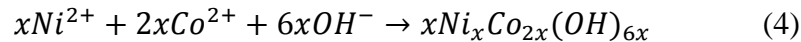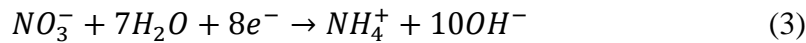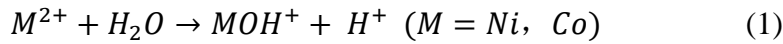**2.6 Electrochemical measurements and preparation of the electrode**

The prepared LDH-MXene electrodes were examined with a three-electrode system in a 6M KOH aqueous electrolyte at ambient temperature. Regarding the working electrode, LDH-MXene electrodes were utilized directly. The counter and reference electrodes were a platinum foil and a saturated calomel electrode (SCE), respectively. An electrochemical working station apparatus (ZIVE SP2) was used for electrochemical impedance spectroscopy (EIS), galvanostatic charge/discharge (GCD) measurements, and cyclic voltammetry (CV). Cycle stability measurements were tested at 30 A g^{-1} for 5000 cycles. CV experiments were executed in the range of 0 and 0.6 V (vs. SCE) at different scan rates. The range of 0- 0.58 V potential (vs. SCE) at different current densities was adjusted for measuring the GCD curves. The measurement of EIS was conducted at a frequency range of 100 kHz to 0.01 Hz at the open circuit potential with a 5 mV AC perturbation. The mean of three sets of independent tests with deviations within $\pm5\%$ for three diverse sets of the specimens were reported.

A SASC device was assembled using MXene-LDH@NF as the positive electrode, MWCNT@NF as the negative electrode and the PVA/KOH gel electrolyte between them. The mass loading for the negative electrode was determined by balancing the charges stored in each electrode. Generally, the charges stored by positive and negative electrode can be determined by $Q_+ = Q_-$, where $Q_+ = C_+ \times \Delta V \times m_+$ and $Q_- = C_- \times \Delta V \times m_-$. In this study, the mass loading of positive and negative electrode was 1.7 mg and 8.1 mg, respectively.

3. Results and discussion

3.1 Fabrication of the MXene-LDH binder-free electrode

The synthesized procedures of the MXene-LDH electrode are presented in Figure 1. First, Ti_3C_2 powders were synthesized by immersing Ti_3AlC_2 into HF solution. The solution was then added to DMSO to obtain the Ti_3C_2 interlayer sheets. The Ti_3C_2 colloidal suspension was loaded onto NF using a simple dropping-mild baking approach without binders because the nanosheet surface was decorated with major hydroxyl groups proposing outstanding hydrophilicity. The last step was electrodeposition of Ni-Co LDHs on in- Ti_3C_2 by the three-electrode system. The shifting current can initiate the process reduction and concurrent deposition reaction of Eqs. (1) and (2) during electrodeposition. Based on a previous report [24, 25], the electrochemical reaction and mixed hydroxide precipitation constitute the whole electrodeposition process of Eqs. (3) and (4).

$$M^{2+} + H_2O \rightarrow MOH^+ + H^+ \ (M = Ni,\ Co) \tag{1}$$

$$MOH^+ + e^- \rightarrow MOH_{ads} \tag{2}$$

$$NO_3^- + 7H_2O + 8e^- \rightarrow NH_4^+ + 10OH^- \tag{3}$$

$$xNi^{2+} + 2xCo^{2+} + 6xOH^- \rightarrow xNi_xCo_{2x}(OH)_{6x} \tag{4}$$

The XRD patterns of MXene, LDH and MXene-LDH are exhibited in Fig. 2. The XRD peaks of LDH at $2\theta=11.5°$, $23.3°$, $34.9°$ and $60.9°$ correspond to the (003), (006), (012) and (110) crystal planes (JCPDS33-0429). MXene-LDH sample shows almost all characteristic peak both of MXene and LDH, shifted left of (003) diffraction peak illustrates the crystal lattice spacing of LDH had increased on account of the intercalation of MXene and electrodeposition, showing that the MXene-LDH structure

is a composite consisting of two phases. And (002) diffraction peak of MXene-LDH shifts to lower angle than for MXene, illustrates the MXene was treated by DMSO which the interlayer spacing expanded [26, 27]. Fig. 2 (b) showed FT-IR spectra of MXene-LDH, MXene and LDH. Compared with pure MXene and LDH, the FT-IR spectrum of MXene-LDH reveals the presence of relevant functional groups. The absorption bands at 3432 and 1628 cm^{-1} can be assigned to the O-H stretching vibration of hydroxyl groups hydrogen bonded in Ni-Co LDH and bending mode of water molecules, respectively. The band at 1384 cm^{-1} belong to the N-O stretching mode of the surface adsorbed nitrate which from the preliminary nickel nitrate hexahydrate and cobalt nitrate hexahydrate. The characteristic IR absorptions peaks confirmed the existence of LDH in the composite.

The chemical composition surface chemical state of the MXene-LDH composited were investigated by X-ray photoelectron spectroscopy (XPS) technique. The XPS survey spectrum of the composite not only Ti 2p and C 1s peaks, but also shows the peaks of Ni 2p, Co 2p and O 1s. (Fig. 3a). The Ni 2p XPS spectrum (Fig. 3b) showed the 2p3/2 and 2p1/2 levels of Ni^{2+} distributed in the main peak of 857 eV and 876 eV, and the XPS spectrum of O 1s (Fig. 3c) showed the peak at 531 eV can be related to hydroxyl ions[28, 29], complement the peak of Ti 2p and C 1s were detected at binding energies of 456 eV and 285 eV, respectively, suggesting the existence of Ni-Co LDH and MXene in the composite.

Figure 4 presents the morphology of the MXene-LDH electrode by SEM and TEM at different magnifications and EDS analysis. SEM images (Figs. 4a and b) demonstrate

that the large numbers of Ni-Co LDH sheets were electrodeposited on the surface of the MXene flake by the interaction between MOH^+ and the functional groups on the surface of MXene, effectively increasing the surface area of the active material and facilitating ion transport. Furthermore, as shown in the TEM images (Figs. 4c and d), the edges of MXene nanosheets were clearly wrapped in Ni-Co LDHs, exhibited distinct different morphology between MXene flake and LDH nanosheet, and obviously extend the surface area on the basic of the original structure. According to the EDS results (Fig. 4e), it can be clearly seen that MXene chemical elements are present in the MXene-LDH composite.

The elemental distribution of the composite was confirmed by energy dispersive spectroscopy (EDS). Table 2 presents the quantitative analysis of the composites as 10.24 wt% C, 9.98 wt% Ti, 17.49 wt% Co, 15.01 wt% Ni, and 43.74 wt% O in the mixture of MXene and Ni-Co LDHs. To further prove the existence of Ni-Co LDH electrodeposited on MXene, the contrast images of the EDS analysis are shown in Fig. 5. The upper part of Fig. 5 (a) is typical of pure Ni-Co LDHs, and the lower part is the mixture of MXene and Ni-Co LDH by electrodeposition. Figures 5 (b), (c), (d), and (e) show the EDS-mapping images of the Ni, Co, Ti and C elements from the sample demonstrated in image Fig. 5 (a), and the result confirms the presence of Ni, Co, Ti, and C elements in the mixture. This result illustrates the chemical component and spatial distribution in the MXene/Ni-Co LDH structure, which demonstrates that the sample is a composite.

Further investigations were performed using TEM/EDS mapping. Figures 6 (a), (b), (c),

and (d) demonstrate the existence of MXene (Ti$_3$C$_2$)-LDHs (NiCo$_2$(OH)$_6$). From Fig. 6 it can clearly be seen the existence of Ti, Ni, and Co elements in the MXene-LDH composition. A selected area electron diffraction (SAED) pattern (Fig. 6 e) reveals hexagonally arranged bright spots confirming the single crystallinity of Ni-Co LDH nanosheet and the diffraction rings reveals the growth of LDH on the surface of the MXene [30, 31].

3.2 Electrochemical Evaluation

C-electrodes were investigated with a three-electrode system for evaluating the electrochemical properties of the binder-free electrode of MXene and Ni-Co LDHs as an active material support on nickel foam for supercapacitors. Figure 7 (a) shows the cyclic voltammetry (CV) curves of the C-electrode with a weight ratio of 3:2, with different scan rates between 5 mV^{-1} and 100 mV^{-1}. A pair of redox peaks was clearly observed for each curve within 0-0.6 V (vs. SCE), corresponding to typical pseudocapacitive behavior. Based on the following reactions (5, 6, and 7), the peaks are attributed to the Ni^{2+}/Ni^{3+} Faradaic redox process [32]:

$$Ni(OH)_2 + OH^- \rightarrow NiOOH + H_2O + e^- \qquad (5)$$

$$CoOOH + OH^- \leftrightarrow CoO_2 + H_2O + e^- \qquad (6)$$

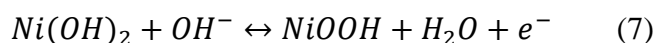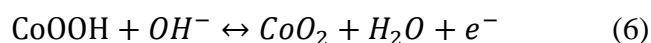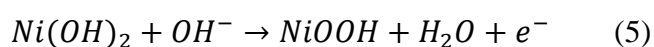$$Ni(OH)_2 + OH^- \leftrightarrow NiOOH + H_2O + e^- \qquad (7)$$

Figure 7 (b) presents the CV curves of different ratio between MXene and LDH at a 5 mV^{-1} scan rate. Compared with pure MXene, the LDH-MXene electrode shows larger integrated areas and higher peak currents, indicating that the latter exhibits a higher specific capacity. The results show that Ni-Co LDH provided a positive effect for the

capacitive performance. The decrease in capacitance retention with repeated cycling is because of the accumulation between the neighboring LDH nanosheets during charge-discharge process that leads to the reduce of pore volume and restrain the charge transport and ions diffusion [33].

As shown in Figs. 7(c) and (d), the galvanostatic charge-discharge (GCD) measurements of MXene-LDH and pure MXene electrodes were conducted at different current densities between 0 and 0.6 V (vs. SCE). The specific capacitance (C_s) values were obtained by the following equation (Eq. 1) based on the discharge curves [34]:

$$C_s = \frac{\int IdV}{vmV} \qquad (1)$$

where C_s, I, Δt, m, v and V are the specific capacity (F/g), the disge current (A), the electrode active material mass (g), the potential scan rate (mV s^{-1}) and the discharge potential interval (V), respectively.

Figure 8 (a) presents the C_s of MXene, LDH, and differently proportioned MXene-LDH binder-free electrodes at numerous current densities. According to the curves, the particular capacitance of the MXene-LDH electrode is greater than that of MXene. Therein, the electrode of the active material mass ratio of MXene and LDH was 3:2, which delivered C_s values of 984, 774, 703, and 629 F g^{-1} at current densities of 2, 6, 10, and 20 A g^{-1}, respectively. Although the C_s values of the pure Ni-Co LDHs electrode were superior to those of the C-electrode at 2 A g^{-1}, the C_s value was reduced from 1435.3 F g^{-1} to 217.3 F g^{-1} with a retention rate of 15.2% when the current density was amplified from 2 to 50 A g^{-1}. For the MXene-LDH electrode, the C value decreased from 983.98 F g^{-1} (at 2 A g^{-1}) to 536.6 F g^{-1}(at 50 A g^{-1}) with a retention rate of 52.4%.

The C_s value of the pure MXene electrode was reduced from 195.7 F g^{-1} (at 2 A g^{-1}) to 89.1 F g^{-1} (at 50 A g^{-1}) with a retention rate of 45.5%. Clearly, compared to the pure LDH electrode and MXene electrode, the C-electrode exhibited excellent electrochemistry performance dependent on MXene for improved electrical conductivity, and LDH improved the specific capacitance.

To determine the ion transport properties of electrode materials for supercapacitor applications, electrochemical impedance spectroscopy (EIS) tests were investigated over frequency ranges of 0.01 Hz to 100 kHz. The Nyquist plots of the MXene-LDH and pure LDH composite electrodes are shown in Fig. 8(b). The proposed equivalent circuit shown in Fig. 8(b) (inset) is the measured impedance. The Nyquist plots of the electrodes consisted of a semicircle curve in the high-frequency region and a straight curve in the low-frequency region [32, 35, 36]. In the high-frequency region, the intercept of the semicircle curve at the real axis (Z_0) is equal to the internal resistance (R_s), which includes the electrolyte resistance, ohmic resistance of the active materials and contact resistance at the active materials/NF interface. The R_s values of the MXene-LDH electrode and pure LDH electrode were 0.28 Ω and 0.33 Ω, respectively. The semicircle which corresponds to double-layer capacitance (C_{dl}) with the surface properties of electrode and its diameter is assigned to the charge transfer resistance (R_{ct}) associated to the involved faradaic reactions at the electrode-electrolyte interface. In the lower frequency area, C_l is the limit capacitance, and the slope of the curves represent the Warburg resistance, which associated to the electrolyte diffusion in the electrodes. As is well known, reduced resistance can efficiently improve the

electrochemical performance for supercapacitors. The EIS result indicates that the LDH nanostructures have a high electrochemical capacity because of their quick and reversible redox reactions at the MXene surface. Three-dimensional MXene guarantees a large surface area and high conductivity of LDH sheets in direct contact with the electrolyte, leading to easy and fast contact of the electrolyte ions with the surface of the electrode materials. Additionally, the binder-free electrodes allow quick electrode-electrolyte interaction and small internal resistance charge transfer.

Figure 9 shows the cycle stability of the MXene-LDH electrode according to the GCD technique at 30 A g^{-1} for 5000 cycles. The initial increase in specific capacity was due to the activation of active material during the initial cycles, and then a slow decrease and capacitance retention remained at approximately 76% at the 5000th cycle. Good cycle stability of carbon materials, such as graphene [37], MXene [38], and CNT [39], has gained significant attention around the world. In this study, comparing with Ni-Co LDHs, the MXene-LDH electrode exhibited better cycle stability and higher current density, the cycle stability of MXene showed a positive impact on the mixture electrode, in which the MXene effectively prevented aggregation of the Ni-Co LDHs during the charge/discharge process.

To further demonstrate the superior capacitive performance of the MXene-LDH on the nickel foam, an asymmetric supercapacitor device was assembled using the MXene-LDH@NF and MWCNT@NF as positive and negative electrodes, respectively. And the prefabricated PVA/KOH gel electrolyte has placed between positive and negative electrodes as a separator (Fig. 10 a). Figure 10b shows the CV curves of MWCNT

electrode and MXene-LDH electrode at a scan rate of 5 mV s^{-1} in a three-electrode test system. The CV curves show that MWCNT (0 ~ -1V) and MXene-LDH (0 ~ 0.6V) electrodes have different potential windows, if they are combined, the potential range of the MXene -LDH//MWCNT SASC device can be extended as much as possible, which is beneficial for improving the electrochemical performance of SASC device. The mass ratio of MXene-LDH to MWCNT was controlled at approximately 0.21 in the SASC device base on the C$_s$ values of MXene-LDH and MWCNT electrode, as well as the principle of charge balance between the electrodes.

Figure 10 (c) present the CV curves of SASC at different scan rate between $0 - 1.6$V, which deviate from a rectangular shape because of the charge storage mechanism of LDH. With the increase in scan rate from 5 mV^{-1} to 100 mV^{-1}, the shape of the CV curves did not change, thereby implying good rapid charge-discharge properties of the device. Figure 10 (d) shown the GCD curves of the asymmetric supercapacitor at various current densities. The energy density (E) and power density (P) values were obtained by the following equations (2 and 3) based on the discharge curves:

$$E = \frac{1}{2}CV^2 \qquad (2)$$

$$P = \frac{E}{\Delta t} \qquad (3)$$

Where E (Wh kg^{-1}) is the energy density, V (V) is the voltage range excluding the IR drop, P (W kg^{-1}) is the average power density, and Δt is the discharge time.

Base on the specific capacity value, the energy density of the MXene-LDH//MWCNT is calculated to 36.70, 30.44, 22.61 and 14.85 Wh kg^{-1} at the power density of 1.44, 2.88, 5.76 and14.40 kW kg^{-1}. The results show that the SASC device achieved higher

energy density than the reported devices (Figure 11). Such as NiCo-LDH@NF//GNS (30.2 Wh kg^{-1} at 800 W kg^{-1}) [32], NiCo$_2$S$_4$@NF//porous carbon(22.8 Wh kg^{-1} at 0.16 kW kg^{-1}) [40], NiCo2O4-rGO//AC (23.3 Wh kg^{-1} at 324.9 W kg^{-1}) [41], Ni$_x$Co$_{1-x}$ LDH@ZTO heterostructure//AC (23.7 Wh kg^{-1} at 284.2 W kg^{-1}) [42], graphene-LDH// AC (35.5 Wh kg^{-1} at 0.875 kW kg^{-1}) [43].

The outstanding electrochemical properties of the MXene-LDH//MWCNT solid-state asymmetric supercapacitor are attributed to the following conditions: 1) Ti$_3$C$_2$ provide express path for rapid electron transport base on the excellent conductivity of carbide materials; 2) the Ni-Co LDH nanoflake structure improve the interfacial contact between the active material and the electrolyte, lead to more efficient charge transportation; 3) the MWCNT@NF negative electrode improve electrolyte accessibility and effective ion-transport pathways, resulting in lower ion-transport resistance.

4. Conclusions

In summary, we synthesized a new binder-free electrode by electrodepositing Ni-Co LDH on the surface of a MXene base on nickel foam that be able to overcome the poor cycling stability (at high current density), low conductivity of LDH-type electrodes, and low specific capacitance of MXene electrodes for supercapacitors. The MXene sheet as a substrate created paths for electron and ion transport, and effectively prevented aggregation of the Ni-Co LDHs during the charge/discharge process. Additionally, the LDH flake deposition on the surface increased the contact area between the active materials and electrolyte and provided Faradaic utilization that led to a high specific capacitance. The specific capacitance value of the optimized ratio

sample was 983.6 F g^{-1} at 2 A g^{-1} and 536.6 F g^{-1} at 50 A g^{-1}, and a capacitance retention

of 76% was attained after 5000 cycles at 30 A g^{-1}. Besides, a solid-state asymmetric

supercapacitor device was fabricated using MXene-LDH@NF as the positive electrode

and MWCNT@NF as the negative electrode, which achieved high energy and power

densities (36.70 Wh kg^{-1} at the power density of 1.44 kW kg^{-1}). In touch with others

deposition methods, these results suggest the composites exhibit promising prospective.

Meanwhile this investigation indicates that other types of LDHs mixed with MXene by

electrodeposition may improve electrode materials for future supercapacitors.

References

[1] M. Hu, Z. Li, H. Zhang, T. Hu, C. Zhang, Z. Wu, X. Wang, Chemical communications, 51 (2015) 13531-13533.
[2] H. Jiang, T. Sun, C. Li, J. Ma, J. Mater. Chem., 22 (2012) 2751-2756.
[3] Y. Zhu, S. Murali, W. Cai, X. Li, J.W. Suk, J.R. Potts, R.S. Ruoff, Advanced materials, 22 (2010) 3906-3924.
[4] T. Brousse, D. Bélanger, J.W. Long, Journal of The Electrochemical Society, 162 (2015) A5185-A5189.
[5] M. Ghidiu, M.R. Lukatskaya, M.Q. Zhao, Y. Gogotsi, M.W. Barsoum, Nature, 516 (2014) 78-81.
[6] M.R. Lukatskaya, O. Mashtalir, C.E. Ren, Y. Dall'Agnese, P. Rozier, P.L. Taberna, M. Naguib, P. Simon, M.W. Barsoum, Y. Gogotsi, Science, 341 (2013) 1502-1505.
[7] D. Sun, M. Wang, Z. Li, G. Fan, L.-Z. Fan, A. Zhou, Electrochemistry Communications, 47 (2014) 80-83.
[8] S.-Y. Lin, X. Zhang, Journal of Power Sources, 294 (2015) 354-359.
[9] F. Wang, C. Yang, C. Duan, D. Xiao, Y. Tang, J. Zhu, Journal of The Electrochemical Society, 162 (2015) B16-B21.
[10] Q. Peng, J. Guo, Q. Zhang, J. Xiang, B. Liu, A. Zhou, R. Liu, Y. Tian, Journal of the American Chemical Society, 136 (2014) 4113-4116.

[11] G.-L. Tian, M.-Q. Zhao, B. Zhang, Q. Zhang, W. Zhang, J.-Q. Huang, T.-C. Chen, W.-Z. Qian, D.S. Su, F. Wei, Journal of Materials Chemistry A, 2 (2014) 1686-1696.

[12] M.D. Levi, M.R. Lukatskaya, S. Sigalov, M. Beidaghi, N. Shpigel, L. Daikhin, D. Aurbach, M.W. Barsoum, Y. Gogotsi, Advanced Energy Materials, 5 (2015) n/a-n/a.

[13] S. Liu, S.C. Lee, U. Patil, I. Shackery, S. Kang, K. Zhang, J.H. Park, K.Y. Chung, S.C. Jun, Journal of Materials Chemistry A, 5 (2017) 1043-1049.

[14] S. Peng, L. Li, H.B. Wu, S. Madhavi, X.W.D. Lou, Advanced Energy Materials, 5 (2015).

[15] Y. Wang, D. Zhang, W. Peng, L. Liu, M. Li, Electrochimica Acta, 56 (2011) 5754-5758.

[16] W. Hong, J. Wang, L. Niu, J. Sun, P. Gong, S. Yang, Journal of Alloys and Compounds, 608 (2014) 297-303.

[17] P. Zhang, B.Y. Guan, L. Yu, X.W.D. Lou, Angewandte Chemie International Edition, 56 (2017) 7141-7145.

[18] Z. Gu, J.J. Atherton, Z.P. Xu, Chemical communications, 51 (2015) 3024-3036.

[19] L. Jiang, Y. Sui, J. Qi, Y. Chang, Y. He, Q. Meng, F. Wei, Z. Sun, Y. Jin, Applied Surface Science, 426 (2017) 148-159.

[20] L. Qian, W. Chen, M. Liu, Q. Jia, D. Xiao, ChemElectroChem, 3 (2016) 950-958.

[21] C. Yuan, J. Li, L. Hou, X. Zhang, L. Shen, X.W.D. Lou, Advanced Functional Materials, 22 (2012) 4592-4597.

[22] X. Li, R. Ding, L. Yi, W. Shi, Q. Xu, E. Liu, Electrochimica Acta, 222 (2016) 1169-1175.

[23] L. Chen, S. Liu, L. Zhao, Y. Zhao, Electrochimica Acta, (2017).

[24] S.B. Kulkarni, A.D. Jagadale, V.S. Kumbhar, R.N. Bulakhe, S.S. Joshi, C.D. Lokhande, International Journal of Hydrogen Energy, 38 (2013) 4046-4053.

[25] G. Wang, L. Zhang, J. Zhang, Chemical Society reviews, 41 (2012) 797-828.

[26] D. Sun, M. Wang, Z. Li, G. Fan, L.-Z. Fan, A. Zhou, Electrochemistry Communications, 47 (2014) 80-83.

[27] Y. Dall'Agnese, M.R. Lukatskaya, K.M. Cook, P.-L. Taberna, Y. Gogotsi, P. Simon, Electrochemistry Communications, 48 (2014) 118-122.

[28] M.C. Biesinger, B.P. Payne, A.P. Grosvenor, L.W. Lau, A.R. Gerson, R.S.C. Smart, Applied Surface Science, 257 (2011) 2717-2730.

[29] J. Pu, Y. Tong, S. Wang, E. Sheng, Z. Wang, Journal of Power Sources, 250 (2014) 250-256.

[30] M. Li, J. Cheng, J. Wang, F. Liu, X. Zhang, Electrochimica Acta, 206 (2016) 108-115.

[31] J. Han, Y. Dou, J. Zhao, M. Wei, D.G. Evans, X. Duan, Small, 9 (2013) 98-106.

[32] L. Zhang, K.N. Hui, K. San Hui, H. Lee, Journal of Power Sources, 318 (2016) 76-85.

[33] L. Zhang, K.N. Hui, K.S. Hui, X. Chen, R. Chen, H. Lee, International Journal of Hydrogen Energy, 41 (2016) 9443-9453.

[34] Y. Bai, W. Wang, R. Wang, J. Sun, L. Gao, Journal of Materials Chemistry A, 3 (2015) 12530-12538.

[35] S. Liu, K.S. Hui, K.N. Hui, V.V. Jadhav, Q.X. Xia, J.M. Yun, Y.R. Cho, R.S.

Mane, K.H. Kim, Electrochimica Acta, 188 (2016) 898-908.

[36] Q.X. Xia, K. San Hui, K.N. Hui, S.D. Kim, J.H. Lim, S.Y. Choi, L.J. Zhang, R.S. Mane, J.M. Yun, K.H. Kim, J. Mater. Chem. A, 3 (2015) 22102-22117.

[37] R.R. Salunkhe, Y.H. Lee, K.H. Chang, J.M. Li, P. Simon, J. Tang, N.L. Torad, C.C. Hu, Y. Yamauchi, Chemistry, 20 (2014) 13838-13852.

[38] M.Q. Zhao, C.E. Ren, Z. Ling, M.R. Lukatskaya, C. Zhang, K.L. Van Aken, M.W. Barsoum, Y. Gogotsi, Advanced materials, 27 (2015) 339-345.

[39] M. Kaempgen, C.K. Chan, J. Ma, Y. Cui, G. Gruner, Nano letters, 9 (2009) 1872-1876.

[40] W. Kong, C. Lu, W. Zhang, J. Pu, Z. Wang, Journal of Materials Chemistry A, 3 (2015) 12452-12460.

[41] X. Wang, W.S. Liu, X. Lu, P.S. Lee, Journal of Materials Chemistry, 22 (2012) 23114-23119.

[42] X. Wang, A. Sumboja, M. Lin, J. Yan, P.S. Lee, Nanoscale, 4 (2012) 7266-7272.

[43] W. Zhang, C. Ma, J. Fang, J. Cheng, X. Zhang, S. Dong, L. Zhang, Rsc Advances, 3 (2013) 2483-2490.

Figure captions

Figure 1 Illustration of the process for preparation of the MXene-LDH electrode.

Figure 2 (a)XRD patterns of MXene-LDH, MXene and LDH, (b) FT-IR spectra of MXene-LDH composite.

Figure 3 XPS spectra of the sample: (a) the survey spectra, (b)-(d) core level spectra of the Ni 2p, O 1s and C 1s region, respectively.

Figure 4 (a,b) SEM and (c,d) TEM images of the MXene-LDH electrode at different magnifications, and the element analysis of the electrode.

Figure 5 Microstructure and chemistry of the MXene/Ni-Co LDH composites. (a)

SEM image of the MXene/Ni-Co LDH composites. The EDS mapping of (b) Ni, (c) Co, (d) Ti, and (e) C.

Figure 6 (a) TEM images of a MXene-LDHs flake. EDS mapping of (b) Ni, (c) Co, and (d) Ti, and (e) SEAD.

Figure 7 (a) CV curves of the MXene:LDH=3:2 electrode at different scan rates, and (b) comparison of the MXene-LDH CV curves at a scan rate of 50 mV. Charge-discharge curves of the (c) MXene-LDH and (d) MXene electrodes at different current densities.

Figure 8 (a) Specific capacitance of MXene, LDH, and different ratios of MXene-LDH, and (b) Nyquist plots of MXene-LDH and LDH electrodes.

Figure 9 Cycle stability of the MXene-LDH, MXene, and LDH electrode at $30A \ g^{-1}$ for 5000 cycles.

Figure 10 (a) Schematic illustration of the SASC device, (b) CV curves of MWCNT and MXene-LDH electrode in three-electrode system at scan rate of $5mV^{-1}$, (c) CV curves of SASC device at different scan rates, (d) Charge-discharge curves at different current densities.

Figure 11 Ragone plot of energy and power density of SASC device at various charge=discharge rates.

HF Etching and DMSO delaminate

hot plate

RE

CE

WE

Ti$_3$AlC$_2$ powders

Ti$_3$C$_2$ colloidal suspension

Ti$_3$C$_2$ loaded on NF

Electrodeposition
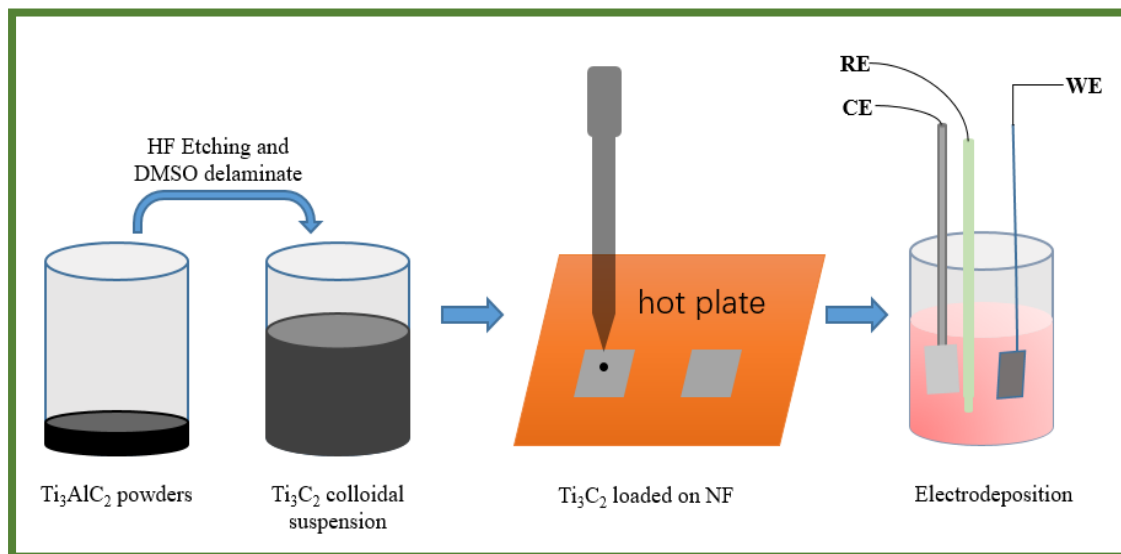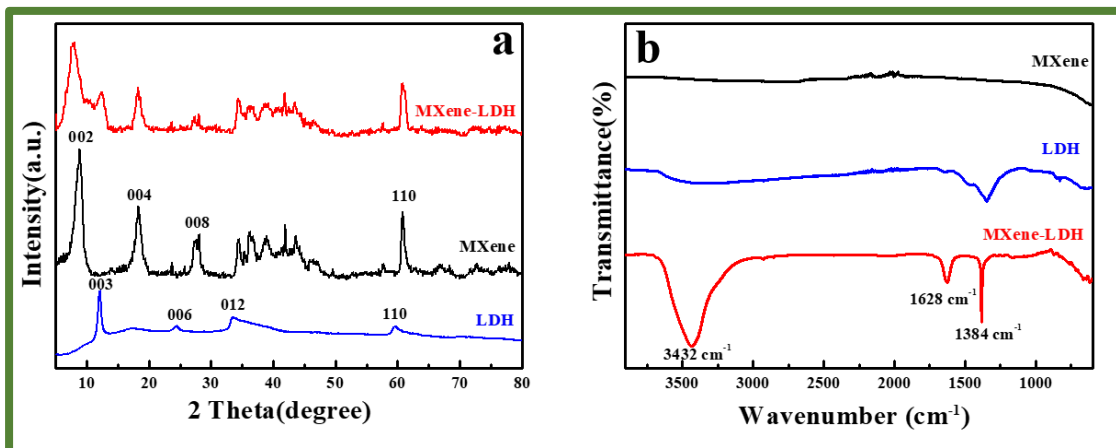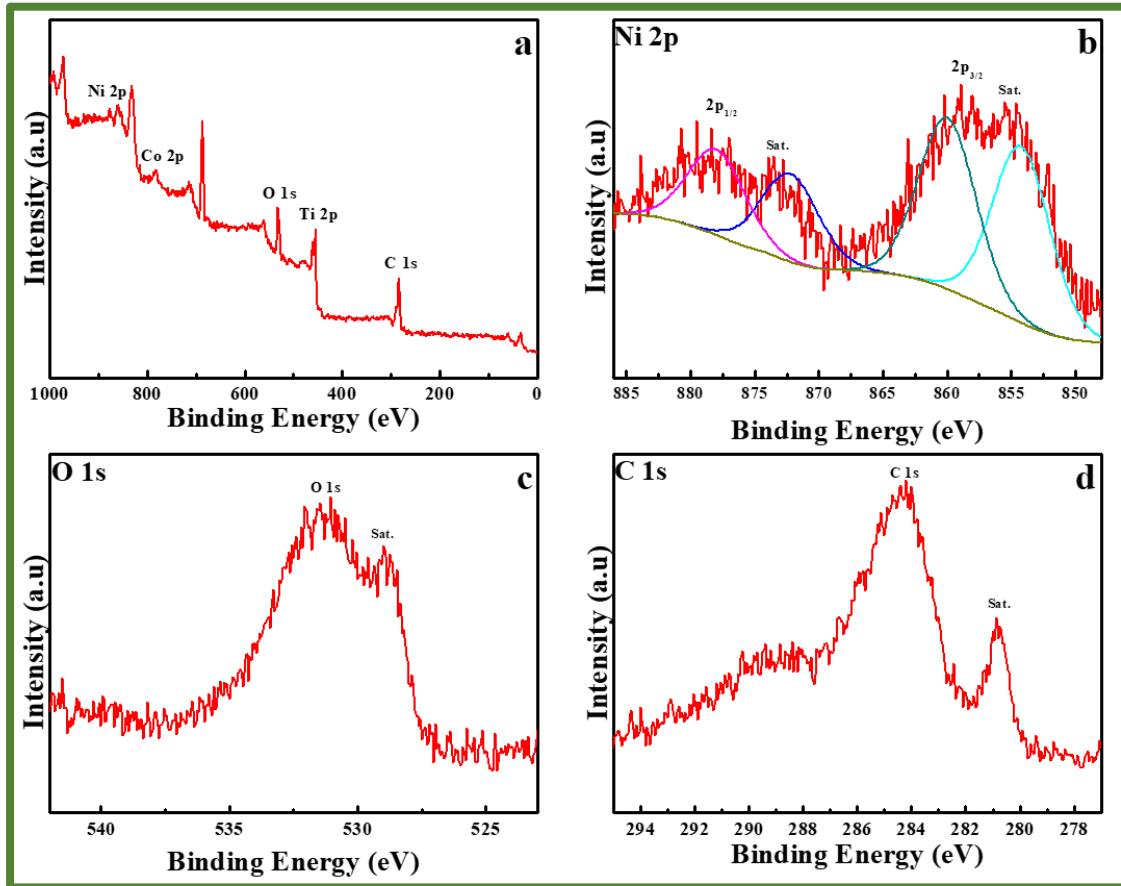
Figure 1

Figure 2

Figure 3
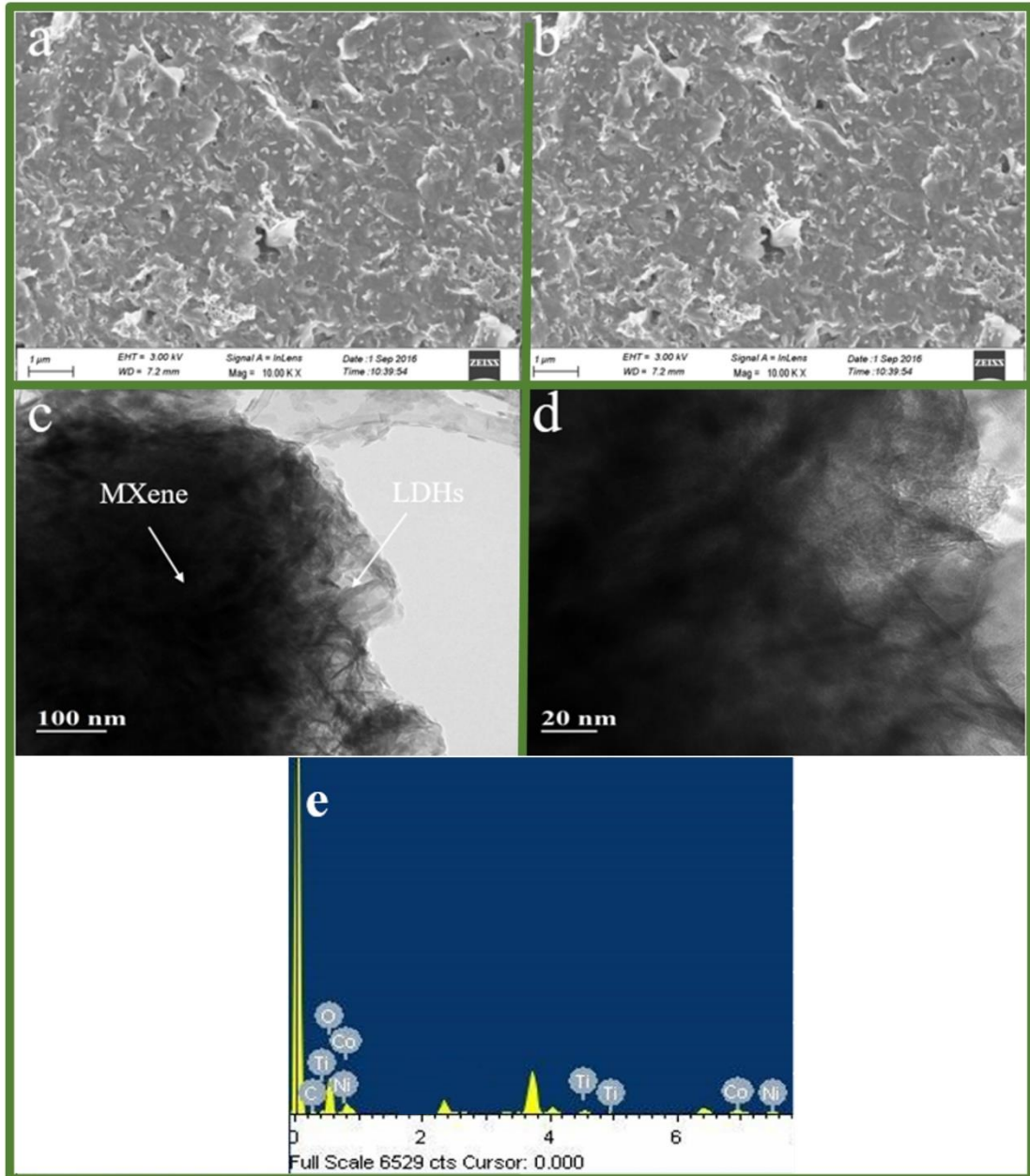
Figure 4
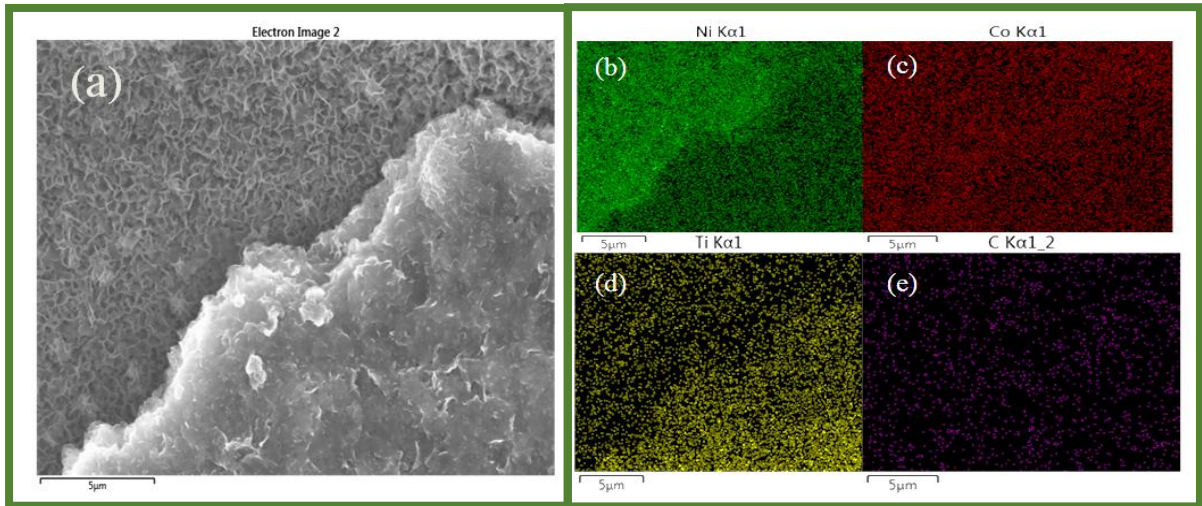
Figure 5
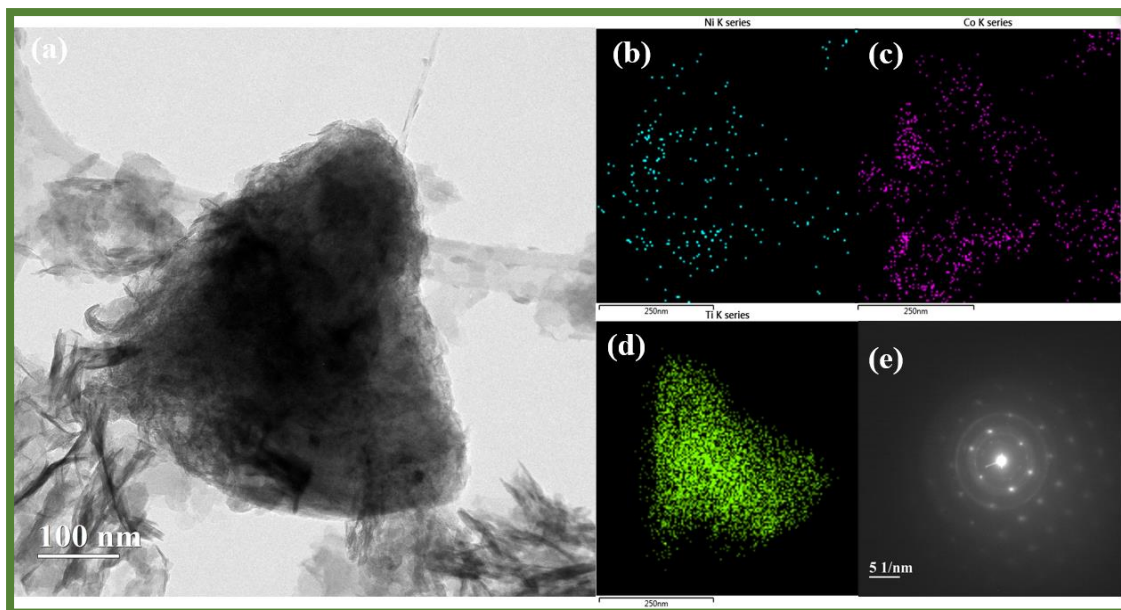
Figure 6
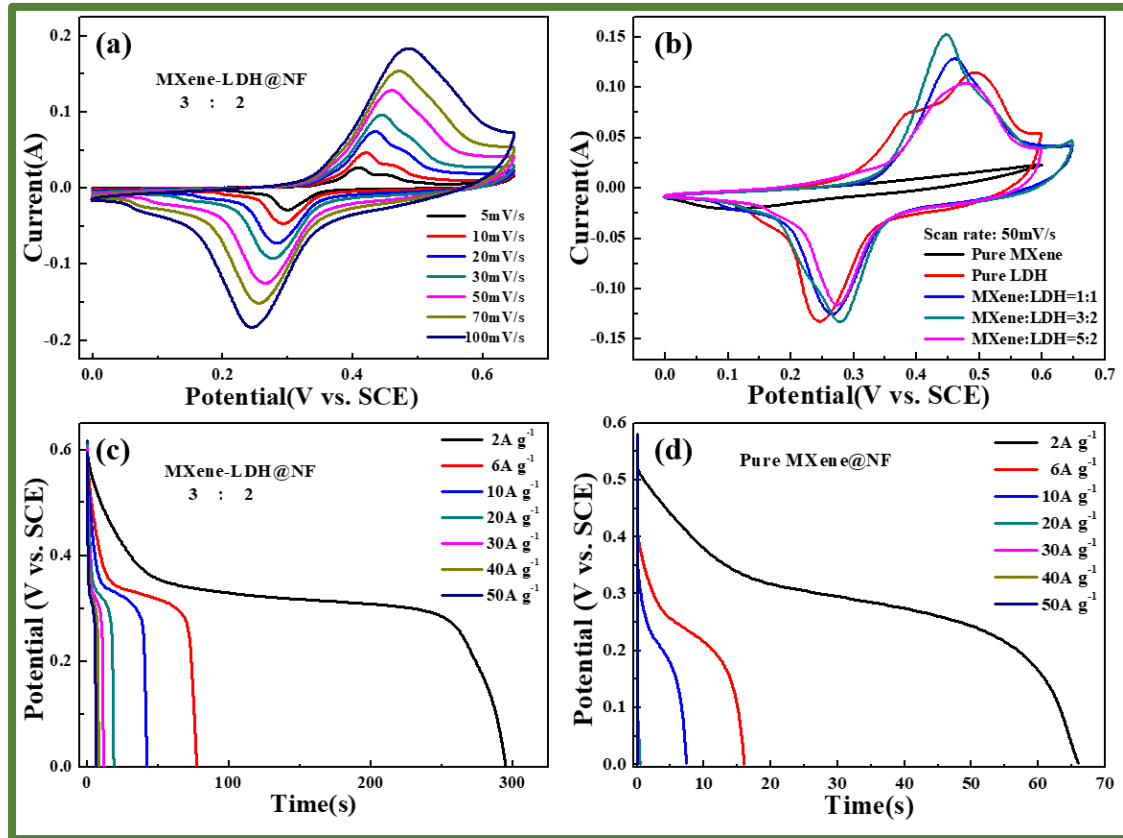
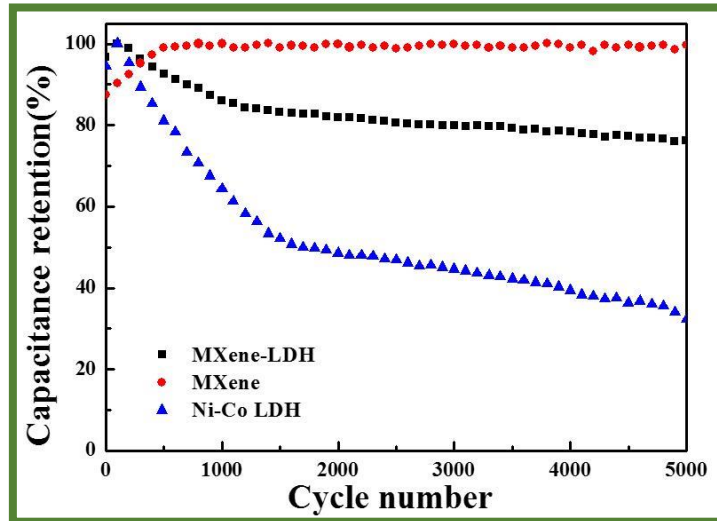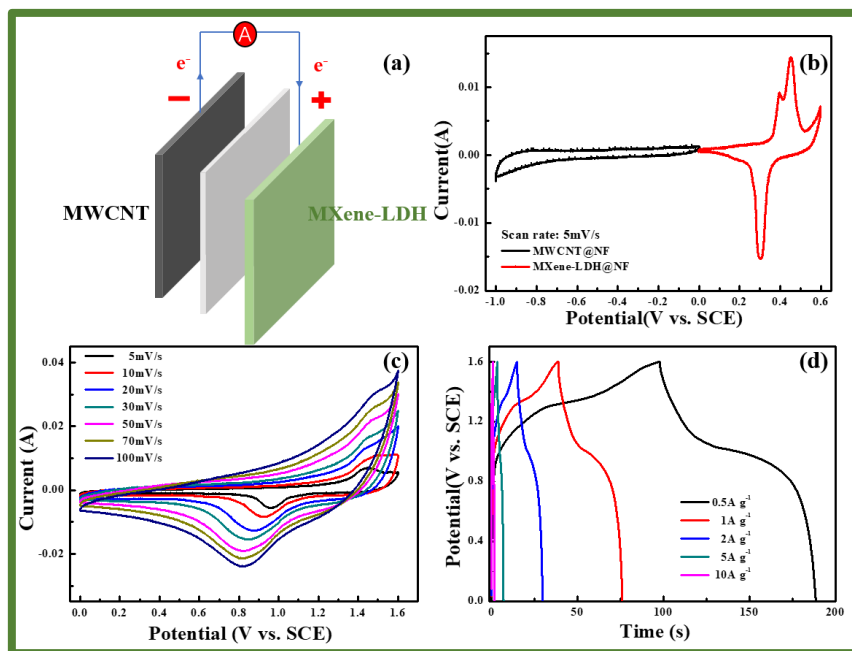**Figure 7**
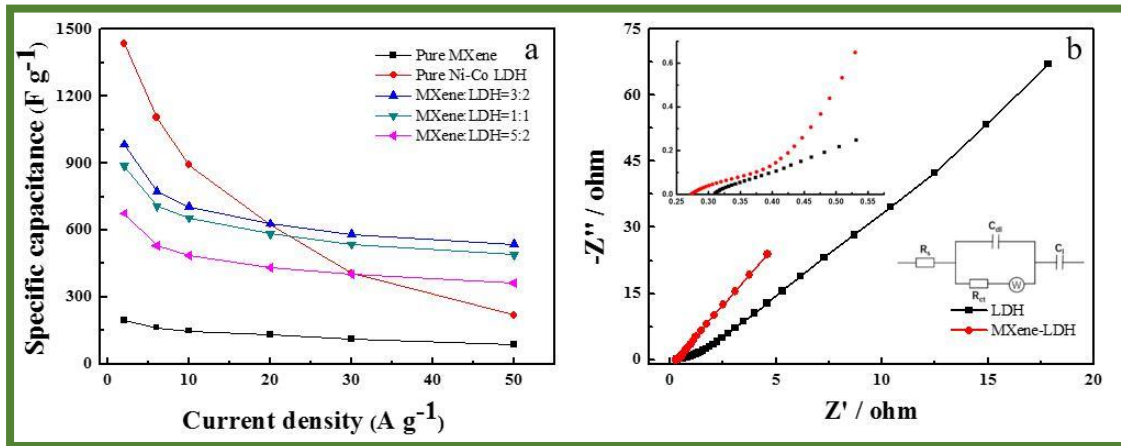
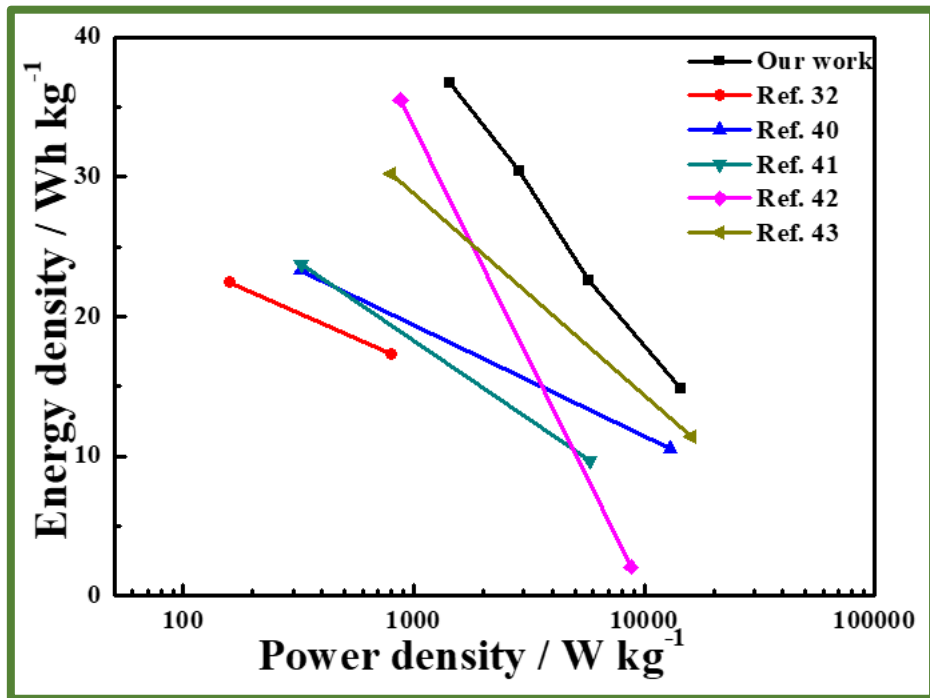**Figure 8**

Figure 9

Figure 10

Figure 11

Table captions
Table 1 The mass loading ratio of active materials
Table 2 Quantitative analysis of EDS in large area
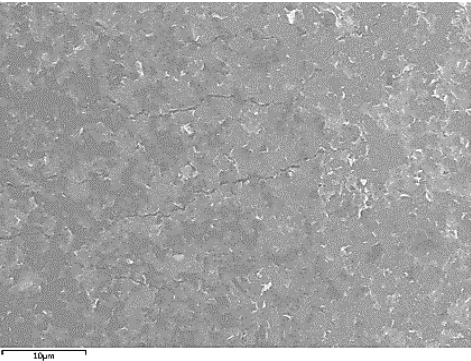
Table 1

Sample	MXene(mg)	LDH(mg)
Pure MXene	1.0	0
Pure Ni-Co LDH	0	1.0
MXene:LDH=1:1	0.5	0.5
MXene:LDH=3:2	0.6	0.4
MXene:LDH=5:2	1.0	0.4

Table 2

Element	Weight%	Atomic%	
C	10.24	9.71	
O	43.74	61.81	
Ti	9.98	9.31	
Co	17.49	9.61	
Ni	15.01	8.70	
Zr	3.55	0.87	
Totals	100.00		